Perpendicular magnetic anisotropy and electrical transport properties of as-deposited $[Pt/Co_2MnSi]_n$ multilayers

Yafan Wan(万雅帆), Bin Kang(康斌), Zeyi Zhu(朱泽镱), Xue Wang(王雪), Xuan Wang(王璇), Luran Zhang(张璐然), Lili Lang(郎莉莉), Li Ma(马丽), Fu Zheng(郑富)

Citation: Chin. Phys. B. 35, 107502 (2026). DOI: 10.1088/1674-1056/ae2676 | CSTR: 32038.14.CPB.ae2676
http://cpb.iphy.ac.cn; http://iopscience.iop.org/cpb

What follows is a list of articles you may be interested in

Magnetic proximity-induced magnetoresistance in $Pt/Tm_3Fe_5O_{12}$ heterostructures

Zhengguo Liang(梁正国), Kunjie Dai(戴坤杰), Qiming Lv(吕崎鸣), Ao Wang(王傲), Jinfeng Zhang(章金凤), Lingfei Wang(王凌飞)

Chin. Phys. B. 35, 077512 (2026). DOI: 10.1088/1674-1056/ae5788 | CSTR: 32038.14.CPB.ae5788

Controlling tilted chiral magnetic textures in Janus Nb*X*Te (*X* = Se, S) monolayers via magnetic field and strain engineering

Xiao-Bo Yu(于晓波), Dong Fan(范栋), Chang-Wen Zhang(张昌文)

Chin. Phys. B. 35, 037504 (2026). DOI: 10.1088/1674-1056/ae3c8a | CSTR: 32038.14.CPB.ae3c8a

Thickness dependence of the magnetic properties of barium ferrite films prepared by pulsed laser deposition

Chengbo Zhao(赵诚博), Bowei Han(韩博纬), Yuchen Zhao(赵宇辰), Yang Sun(孙洋), Lichen Wang(王利晨), Ruoshui Liu(刘若水), Yunzhong Chen(陈允忠), Dengjing Wang(王登京)

Chin. Phys. B. 35, 027504 (2026). DOI: 10.1088/1674-1056/adf6a5 | CSTR: 32038.14.CPB.adf6a5

Coupling of magnon modes in nanodisk with spin texture

Zijie Zhou(周子杰), Junning Zhao(赵俊宁), Xinhui Ma(马心慧), Rong Wang(王熔), Fusheng Ma(马付胜)

Chin. Phys. B. 34, 107506 (2025). DOI: 10.1088/1674-1056/ade426 | CSTR: 32038.14.CPB.ade426

Direct observation of ultrafast magnetization dynamics in Co/Ni bit patterned media by time-resolved scanning Kerr microscopy

Wei Zhang(张伟), Wei He(何为), Qin-Li Lv(吕琴丽), Jian-Wang Cai(蔡建旺), Xiang-Qun Zhang(张向群), Zhao-Hua Cheng(成昭华)

Chin. Phys. B. 34, 047501 (2025). DOI: 10.1088/1674-1056/adb67e | CSTR: 32038.14.CPB.adb67e

---

Perpendicular magnetic anisotropy and electrical transport properties of as-deposited $[Pt/Co_2MnSi]_n$ multilayers

Yafan Wan(万雅帆)[1], Bin Kang(康斌)[1], Zeyi Zhu(朱泽镱)[1], Xue Wang(王雪)[1], Xuan Wang(王璇)[2], Luran Zhang(张璐然)[3], Lili Lang(郎莉莉)[4], Li Ma(马丽)[1,†], and Fu Zheng(郑富)[1,‡]

[1] *School of Physics, Ningxia University, Yinchuan* 750021, *China*
[2] *Department of Physics, School of Science, Lanzhou University of Technology, Lanzhou* 730050, *China*
[3] *School of Materials and Energy, Yunnan University, Kunming* 650091, *China*
[4] *Shanghai Institute of Microsystem and Information Technology, Chinese Academy of Sciences, Shanghai* 200050, *China*

(Received 11 October 2025; revised manuscript received 20 November 2025; accepted manuscript online 2 December 2025)

In pursuit of ultra-high-density and stable data storage devices, film materials with perpendicular magnetic anisotropy (PMA) are highly desirable. The exploitation of interfacial effects to induce PMA in heavy metal/ferromagnetic multilayers has become a major research focus. In this study, the PMA and electrical transport properties of Ta (6 nm)/[Pt (2 nm)/Co_2MnSi (t_{CMS} nm)]$_n$/Pt (4 nm) multilayers in the as-deposited state were systematically investigated, with particular focus on the effects of ferromagnetic layer thickness ($t_{CMS} = 0.50$ nm–1.50 nm) and the number of periods ($n = 1$–8). All samples were fabricated by magnetron sputtering and were not subjected to any annealing process. The magnetic results show that the multilayers exhibit PMA when the Co_2MnSi thickness $t_{CMS} \leq 1.00$ nm. Notably, an effective magnetic anisotropy constant $K_{eff} = 1.90 \times 10^6$ erg/cm^3 (1 erg $= 10^{-7}$ J) is achieved for the sample with $t_{CMS} = 0.75$ nm and $n = 3$. Additionally, the phonon scattering mechanism was found to be the dominant contribution to the anomalous Hall effect (AHE) in our studied multilayers. These Co_2MnSi-based multilayers are promising candidates for spintronic devices due to their robust PMA and tunable interfacial effects, which are essential for high storage density and low-power operation.

Keywords: $[Pt/Co_2MnSi]_n$ multilayers, perpendicular magnetic anisotropy, anomalous Hall effect, interfacial effects

PACS: 75.30.Gw, 75.70.–i, 75.70.Cn, 73.61.–r

DOI: 10.1088/1674-1056/ae2676 **CSTR:** 32038.14.CPB.ae2676

1. Introduction

In the rapidly evolving field of information technology, the development of ultra-high-density, low-power, and highly stable data storage devices has emerged as a central focus of research. Thin film materials with robust perpendicular magnetic anisotropy (PMA) have attracted considerable attention due to their critical role in spintronic memory devices, such as magnetic tunnel junctions (MTJs) and spin–orbit torque magnetic random-access memory (SOT-MRAM).[1–3] These films exhibiting PMA stabilize the out-of-plane magnetization direction, thereby significantly increasing the storage density while simultaneously improving both the reliability and thermal stability of data memory cells. Meanwhile, the anomalous Hall effect (AHE), a paradigmatic spin–orbit coupling (SOC) transport phenomenon, serves as a critical enabler for high-sensitivity magnetic sensors and spin-based logic devices.[4–6] The synergistic optimization of PMA and the AHE is of significant technological importance. PMA enables stable, high-density magnetic domains through an out-of-plane easy axis, greatly improving the thermal stability and switching reliability of memory cells. Concurrently, a highly responsive AHE provides an efficient electrical readout mechanism by converting magnetization orientation into a transverse voltage signal. Consequently, the interplay between PMA and AHE represents a key focus in the development of advanced spintronic devices.

In recent years, multilayer structures based on ferromagnetic/heavy metal (FM/HM)[7–11] and ferromagnetic/oxide (FM/OX)[12–19] heterostructures have emerged as mainstream systems for investigating PMA. The FM/HM interface can host magnetic proximity effects, Rashba-type spin–orbit fields, and gate-tunable SOC. These interfacial phenomena govern both the magnitude and symmetry of PMA and determine the electronic transport properties, including the AHE, the spin Hall effect (SHE), and other spin-dependent transport signatures.[14–16,20–23] Specifically, the PMA in these systems primarily originates from symmetry breaking at the interfaces, which results in orbital hybridization, particularly the strong SOC between the 5d electrons of heavy metal layers (*e.g.*, Pt, Pd, Ta) and the 3d electrons of ferromagnetic layers (*e.g.*, Co, Fe).[24–28] The PMA performance can be effectively enhanced through the modulation of interfacial interactions, such as in-

†Corresponding author. E-mail: mali2022@nxu.edu.cn
‡Corresponding author. E-mail: zhengfu@nxu.edu.cn

© 2026 Chinese Physical Society and IOP Publishing Ltd. All rights, including for text and data mining, AI training, and similar technologies, are reserved.

creasing the number of heterostructures or promoting interfacial orbital hybridization. However, conventional PMA materials (*e.g.*, Co/Pt, Co/Pd, and Co/Ni)[29–36] exhibit strong PMA but are generally associated with low spin polarization, which limits their potential for further reduction of the threshold current density in spintronic devices. Therefore, the development of novel material systems that combine high spin polarization with tunable PMA characteristics has emerged as a key direction for achieving breakthroughs in the field.

Half-metallic Heusler alloys, such as Co_2MnSi (CMS), are regarded as promising candidates for MTJ electrodes due to their theoretically predicted 100% spin polarization and low magnetic damping coefficients.[37,38] However, their cubic crystal structure inherently results in weak magnetocrystalline anisotropy, making it challenging to achieve strong PMA in single-layer Co-based alloy thin films. To overcome this limitation, interface-induced PMA can be introduced in heterostructures of Heusler alloys with heavy metals (*e.g.*, Pt) or oxides (*e.g.*, MgO). For instance, in Pt/Co_2MnSi multilayer structures, the strong SOC of Pt induces hybridization between the Pt 5d and Co 3d orbitals at the interface,[27] thereby breaking symmetry and giving rise to PMA oriented normal to the film plane. At present, ferromagnetic Heusler alloy films with PMA exhibit a large AHE, arising from their high spin polarization and strong SOC. In such systems, the magnetotransport behavior is often dominated by exchange splitting, with Zeeman splitting playing a relatively minor role. Furthermore, periodic multilayer architectures can accumulate interfacial orbital hybridization effects by the repeated stacking of FM/HM interfaces, thereby enhancing the effective magnetic anisotropy constant K_{eff}. Studies have shown that PMA is strongly influenced by the thickness of the ferromagnetic layer,[15] the number of periods,[7] the design of buffer or capping layers,[12] as well as the deposition conditions.[9] For example, when the ferromagnetic layer is too thick, the in-plane cubic anisotropy of the bulk material gradually dominates, leading to the suppression of PMA. Conversely, although increasing the number of periods can lead to an enhancement of interfacial anisotropy energy, excessive periodicity may cause the magnetic moments to deviate from the perpendicular direction due to enhanced demagnetizing fields or the accumulation of interfacial defects.

In this context, to address the practical requirements of spintronic devices such as SOT-MRAM, it is essential to develop PMA materials with high spin polarization, low coercivity, and superior interfacial quality.[16,39–42] Here, we integrate the high spin polarization of Co_2MnSi Heusler alloy with the interfacial PMA modulation mechanism of HM/FM heterostructures to optimize spintronic device performance. We demonstrate robust PMA in Ta/$[Pt/CMS]_n$/Pt multilayers without any annealing process, a significant advantage for device integration. Furthermore, analysis of the electrical transport properties reveals the mechanisms governing the AHE in such multilayer systems. This work offers insights into the design of spintronic devices based on Heusler alloy multilayer systems.

2. Experimental details

Figure 1(a) shows a schematic illustration of the multilayer thin film structure studied in this study. The samples were fabricated via layer-by-layer deposition on a single-crystal Si/SiO_2 substrate and exhibit a nominal configuration of Ta (6 nm)/[Pt (2 nm)/CMS (t_{CMS} nm)]$_n$/Pt (4 nm). Here, t_{CMS} refers to the thickness of the ferromagnetic CMS layer, and n denotes the number of repeating Pt/CMS bilayers. A 6-nm-thick Ta layer was deposited onto a single-crystal Si/SiO_2 substrate as an adhesion layer, while a 4-nm-thick heavy metal Pt layer, serving as a protective capping layer, was deposited as the outermost layer of the multilayer stack. This Pt layer also interacts with the CMS layer to induce PMA. All samples were fabricated using an ultra-high-vacuum magnetron sputtering system (Kurt J. Lesker Company, PVD 75 Proline). The base pressure in the sputtering chamber was maintained below 1.0×10^{-8} Torr (1 Torr = 1.33322×10^2 Pa). During deposition, the sputtering pressure was kept at 4 mTorr using high-purity argon (Ar) gas with a purity of 99.99%. The Ar flow rate was maintained at 23 sccm (sccm denotes cubic centimeter per minute at standard temperature and pressure). To ensure uniform deposition and a homogeneous film thickness, the substrate holder was rotated at 10 rpm during sputtering. The Ta, Pt, and CMS targets used for deposition had a purity of greater than 99.9%. The CMS target was an alloy with a nominal composition of $Co_{50}Mn_{25}Si_{25}$ (in atomic percentage). The sputtering parameters used for each target are listed in Table 1. The Ta and CMS targets were sputtered using a DC power supply at 25 W and 10 W, respectively, while the Pt target was deposited using an RF power supply at 50 W. It should be noted that all samples were prepared at room temperature.

The thickness of each layer was characterized using an atomic force microscope (AFM, Benyuan, CSPM 5500). The in-plane and out-of-plane hysteresis loops of the samples were measured at room temperature using a vibrating sample magnetometer (VSM, MicroSense, EZ9). The surface roughness was evaluated by x-ray reflectivity (XRR, Rigaku, SmartLab SE) measurements. The transport properties were measured using a Hall effect measurement system (Lanhai Science Instrument, LH8800 series) across a temperature range from 5 K to 300 K. A shadow mask was employed during the film deposition to enable the *in situ* fabrication of Hall bar devices for subsequent electrical transport measurements, as shown in Fig. 1(b). During the measurement, a magnetic field was applied perpendicular to the film plane. A current of 0.1 mA was

supplied across the longitudinal direction (*xx* direction) of the Hall bar devices, and both the transverse voltage V_{xy} and longitudinal voltage V_{xx} were recorded. The Hall resistivity ρ_{xy} and longitudinal resistivity ρ_{xx} were subsequently calculated based on the measured voltage signals and device geometry.

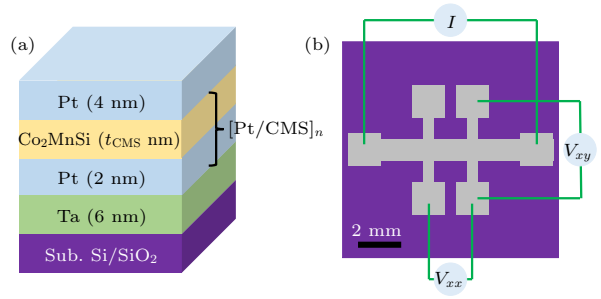

Fig. 1. Schematic illustration of (a) the multilayer structure and (b) the Hall bar device used for electrical transport measurements.

Table 1. Sputtering parameters of the employed targets.

Targets	Power supply type	Sputtering pressure (mTorr)	Power (W)	Ar flow rate (sccm)
Ta	DC	4	25	23
Pt	RF	4	50	23
CMS	DC	4	10	23

3. Results and discussion

The in-plane and out-of-plane hysteresis loops of the as-deposited Ta (6 nm)/[Pt (2 nm)/CMS (t_{CMS} nm)]$_n$/Pt (4 nm) multilayers are shown in Fig. 2. The CMS thickness t_{CMS} is varied from 0.50 nm to 1.50 nm in 0.25-nm increments. The results reveal that PMA is observed for $n = 1$ to 3 when $t_{CMS} \leq 1.00$ nm. Notably, an increase in the number of bilayer periods from $n = 1$ to 3 in the multilayers leads to a significant improvement in the magnetic properties, which is reflected in the improved remanence ratio M_r/M_s of the out-of-plane hysteresis loops, indicating a stronger PMA. This can be attributed to enhanced interfacial orbital hybridization and the cumulative effect of SOC. As shown in Fig. 2(g), for the multilayer with $n = 3$ and $t_{CMS} = 0.75$ nm, the out-of-plane hysteresis loop exhibits M_r/M_s of approximately 1. Meanwhile, the multilayer shows a high saturation magnetization ($M_s \approx 788.7$ emu/cm^3) and a low coercivity ($H_c \approx 10$ Oe, 1 Oe = 79.5775 A·m^{-1}), which facilitates magnetization switching and is advantageous for low-power spintronic devices. In stark contrast, the in-plane hysteresis loop exhibits a nearly linear magnetization behavior and a saturation field as high as 4 kOe. These observations confirm that the perpendicular direction is the easy magnetization axis. As the CMS thickness increases, both the $n = 1$ and $n = 3$ films gradually transition from PMA to in-plane magnetic anisotropy (IMA), and all films exhibit IMA when $t_{CMS} \geq 1.25$ nm. This behavior is attributed to the weakening of interfacial orbital hybridization with increasing thickness of the ferromagnetic layer, which enables the in-plane cubic anisotropy of the bulk material to become dominant.[43] Additionally, as the CMS thickness increases, the exchange coupling between the Pt and CMS layers in the multilayer structure weakens, resulting in a transition of the magnetic anisotropy toward an in-plane orientation.

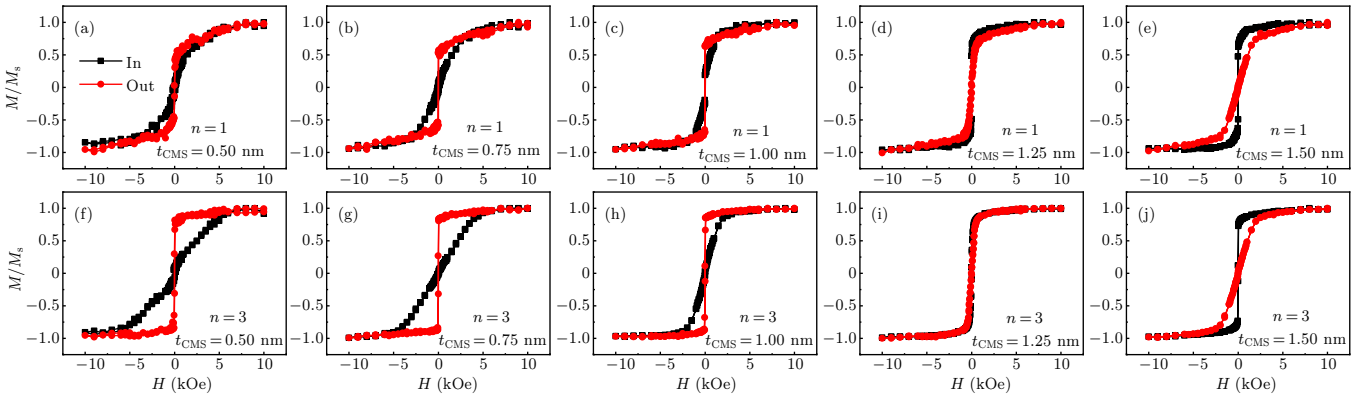

Fig. 2. In-plane and out-of-plane hysteresis loops of Ta (6 nm)/[Pt (2 nm)/CMS (t_{CMS} nm)]$_n$/Pt (4 nm) multilayers with $n = 1$ [(a)–(e)] and $n = 3$ [(f)–(j)]. Each panel corresponds to a different CMS thickness: (a) and (f) 0.50, (b) and (g) 0.75, (c) and (h) 1.00, (d) and (i) 1.25, and (e) and (j) 1.50 nm. All samples were measured in the as-deposited state.

To quantify the magnetic anisotropy of multilayers, the effective magnetic anisotropy constant K_{eff} is commonly employed. The K_{eff} accounts for the contributions of various anisotropic factors, including magnetocrystalline anisotropy, shape anisotropy, and interfacial anisotropy. It can be expressed as follows:[44]

$$K_{eff} = K_v - 2\pi M_s^2 + \frac{K_i}{t}, \quad (1)$$

where K_v represents the volume magnetic anisotropy constant, K_i denotes the interfacial magnetic anisotropy constant, M_s is the saturation magnetization, and the term $-2\pi M_s^2$ corresponds to the demagnetizing energy. The total thickness of the ferromagnetic layer is represented by t_{CMS}. The K_{eff} of the film can be determined by integrating the area difference between the hysteresis loops measured under magnetic fields applied perpendicular (out-of-plane) and parallel (in-plane) to

the film plane, as follows:[45]

$$K_{\rm eff} = \int_0^{M_{\rm s}} H_{\parallel}\,{\rm d}M - \int_0^{M_{\rm s}} H_{\perp}\,{\rm d}M, \tag{2}$$

where $H_{\parallel}$ denotes the magnetic field applied parallel to the film plane (used to obtain the in-plane hysteresis loop), and $H_{\perp}$ represents the field applied perpendicular to the film plane (for the out-of-plane hysteresis loop). Generally, when $K_{\rm eff}$ is positive, the easy axis of magnetization is oriented perpendicular to the film plane, indicating PMA. Conversely, a negative $K_{\rm eff}$ value corresponds to an in-plane easy axis, and the film exhibits IMA. As the thickness of the ferromagnetic layer increases, the demagnetizing energy of the multilayers gradually increases, while the interfacial anisotropy energy decreases, leading to a reduction in the $K_{\rm eff}$. For both $n = 1$ and $n = 3$, when the CMS thickness is in the range of 0.50 nm to 1.00 nm, $K_{\rm eff} > 0$, indicating PMA. In contrast, when $t_{\rm CMS} \geq 1.25$ nm, $K_{\rm eff} < 0$, corresponding to IMA. Specifically, for the multilayer with $n = 3$ and $t_{\rm CMS} = 0.75$ nm, $K_{\rm eff} = 1.90 \times 10^6$ erg/cm^3. By calculating $K_{\rm eff}$ for different thicknesses of the ferromagnetic layer and fitting the results to the following equation

$$K_{\rm eff} \times t = (K_{\rm v} - 2\pi M_{\rm s}^2) \times t + K_{\rm i}, \tag{3}$$

the net volume anisotropy $K_{\rm v} - 2\pi M_{\rm s}^2$ and the $K_{\rm i}$ can be obtained. This equation describes the linear relationship between the dependent variable $K_{\rm eff} \times t$ and the independent variable t, where t represents the total thickness of the CMS layer. $K_{\rm i}$ corresponds to the y-intercept of the fitted line.

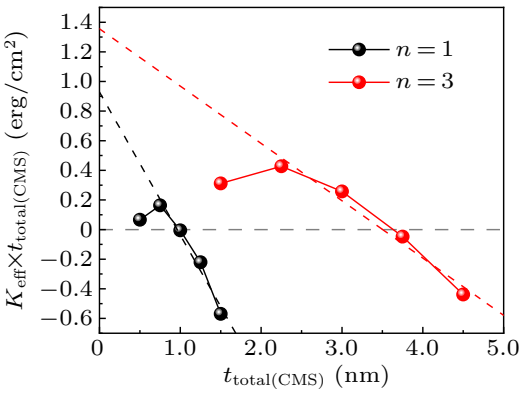

Fig. 3. Dependence of $K_{\rm eff} \times t_{\rm total(CMS)}$ on total CMS thickness.

As shown in Fig. 3, for a single period ($n = 1$), $K_{\rm i} = 0.93$ erg/cm^2, while for $n = 3$, $K_{\rm i}$ increases to 1.36 erg/cm^2, representing a 46.2% enhancement compared to the $n = 1$ case. This result indicates that interfacial anisotropy can be markedly enhanced by employing periodic multilayer structures. In the Ta (6 nm)/[Pt (2 nm)/CMS ($t_{\rm CMS}$ nm)]$_n$/Pt (4 nm) multilayer system, the PMA primarily originates from the SOC at the interface between the heavy metal Pt and the CMS layer. The strong SOC in Pt promotes the hybridization between the Pt 5d and Co 3d orbitals at the interface, thereby reducing the interfacial symmetry and inducing magnetic anisotropy perpendicular to the film plane.[31] These results reveal that increasing the number of periods n leads to an increase in the number of FM/HM interfaces, which enhances $K_{\rm i}$, elevates $K_{\rm eff}$, and ultimately strengthens the PMA of the multilayers.

To evaluate the structural integrity and surface roughness of the multilayer stack, XRR measurements were performed on samples with $n = 3$ and $t_{\rm CMS} = 0.75$ nm and 1.00 nm. As shown in Fig. 4, the experimental data are in good agreement with the best-fit simulation, indicating that the assumed layer stack and interfacial parameters are physically reasonable. While interfacial roughness is independently fitted for each internal layer, film flatness is characterized by the surface roughness (top Pt/air interface), which is 0.53 nm and 0.54 nm for $t_{\rm CMS} = 0.75$ nm and 1.00 nm, respectively. These results indicate coherent layer-by-layer growth, and the resulting smooth, well-defined interfaces are essential for achieving strong PMA.

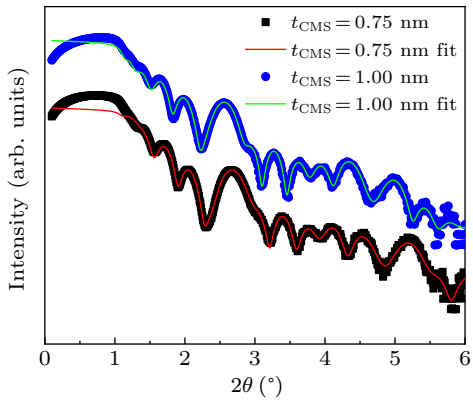

Fig. 4. Experimental XRR curves (symbols) and corresponding best-fit simulations (solid lines) for Ta (6 nm)/[Pt (2 nm)/CMS ($t_{\rm CMS}$ nm)]$_3$/Pt (4 nm) multilayers with $t_{\rm CMS} = 0.75$ nm and 1.00 nm.

The magnetization state of the multilayers was further characterized using AHE, which offers higher sensitivity to magnetic signals in the samples. Accordingly, Hall bar devices, as shown in Fig. 1(b), were fabricated to perform transport measurements for determining the Hall and longitudinal resistivities, ρ_{xy} and ρ_{xx}. The preceding magnetic characterization results demonstrate that multilayers with $n = 3$ and CMS thicknesses of 0.75 nm and 1.00 nm exhibit strong PMA. Hall bar-shaped multilayers with the two selected CMS thicknesses were fabricated and subjected to AHE measurements at temperatures of 5, 50, 100, 150, 200, 250, and 300 K. A magnetic field was applied perpendicular to the film plane during transport measurements and swept between −3000 Oe and +3000 Oe. As shown in Fig. 5, both multilayers with $t_{\rm CMS} = 0.75$ nm and 1.00 nm exhibit robust PMA across all tested temperatures, consistent with the hysteresis loop results. The coercivity of both multilayer structures decreases with increasing temperature. For instance, as shown in Fig. 5(b), the

multilayer with $t_{CMS} = 1.00$ nm exhibits a strong temperature dependence of coercivity, decreasing from 385.8 Oe at 5 K to 12.7 Oe at 300 K. This trend can be attributed to the suppression of thermal fluctuations at low temperatures. The reduced thermal energy makes it difficult for magnetic moments to overcome pinning barriers, thereby requiring a larger external field for magnetization reversal and resulting in higher coercivity.[46] As the temperature increases, thermal fluctuations enable magnetic moments to overcome pinning barriers more easily, thereby reducing the external field strength required for magnetization reversal.

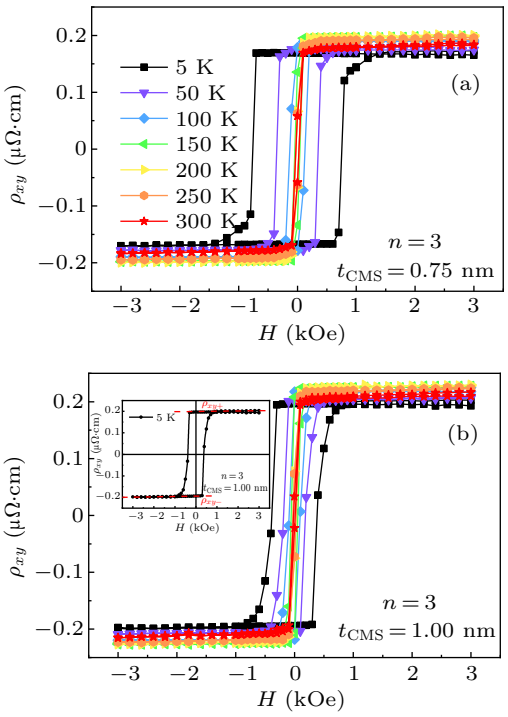

Fig. 5. ρ_{xy}–H curves of Ta (6 nm)/[Pt (2 nm)/CMS (t_{CMS} nm)]$_3$/Pt (4 nm) Hall bars with $t_{CMS} = 0.75$ nm (a) and 1.00 nm (b), measured at temperatures ranging from 5 K to 300 K. The inset in panel (b) illustrates how ρ_{xy+} and ρ_{xy-} are obtained.

Figure 6(a) presents the variation of ρ_{xx} with temperature for Ta/[Pt/CMS]$_3$/Pt multilayers with CMS thicknesses of 0.75 nm and 1.00 nm. As the CMS thickness increases from 0.75 nm to 1.00 nm, ρ_{xx} exhibits an increase for all measured temperatures. This is mainly attributed to the fact that the resistivity of CMS is significantly larger than that of Pt and Ta. Furthermore, the results show that ρ_{xx} increases monotonically with temperature for both samples. This trend is attributed to the fact that, as a half-metal, CMS exhibits temperature-dependent resistivity primarily governed by electron–phonon scattering. As temperature increases, the amplitude of lattice vibrations (phonon population) rises, thereby enhancing electron–phonon scattering and leading to an increase in ρ_{xx}.

In 1930, Pugh *et al*. derived an empirical formula through repeated experiments:[5,47]

$$\rho_{xy} = R_0 H + 4\pi R_s M_z, \tag{4}$$

where R_0 is the ordinary Hall coefficient, H is the magnetic field strength, R_s is the anomalous Hall coefficient, and M_z denotes the spontaneous magnetization perpendicular to the film plane. In ferromagnetic films, a sufficiently large magnetic field applied perpendicular to the film plane fully magnetizes the film. As the external field is increased beyond saturation, ρ_{xy} becomes linearly proportional to the applied field. The anomalous Hall resistivity ρ_{AH} is obtained by extrapolating ρ_{xy} at high magnetic fields to zero magnetic field. The intercept at $H = 0$ gives ρ_{AH}, and the slope of the extrapolated line is R_0. Note that independent linear fits are performed on the high-field regions for positive and negative magnetic fields to obtain ρ_{xy+} and ρ_{xy-} (as shown in the inset of Fig. 5(b)), and ρ_{AH} is calculated as $\rho_{AH} = (\rho_{xy+} - \rho_{xy-})/2$.

As shown in Fig. 6(b), ρ_{AH} exhibits a non-monotonic dependence on temperature. At low temperatures, phonon thermal vibrations are suppressed, and electron scattering is therefore dominated by interfacial impurities and lattice defects. With increasing temperature, enhanced phonon scattering gives rise to an initial increase in ρ_{AH}. However, as the temperature increases further, ρ_{AH} decreases, mainly due to the reduction in magnetization of the ferromagnetic layers induced by this temperature rise. Therefore, ρ_{AH} exhibits a non-monotonic temperature dependence, characterized by an initial increase followed by a pronounced decrease. Additionally, increasing the CMS layer thickness from 0.75 nm to 1.00 nm results in a higher ρ_{AH}, which is attributed to the accumulation of interfacial defects and enhanced phonon scattering.

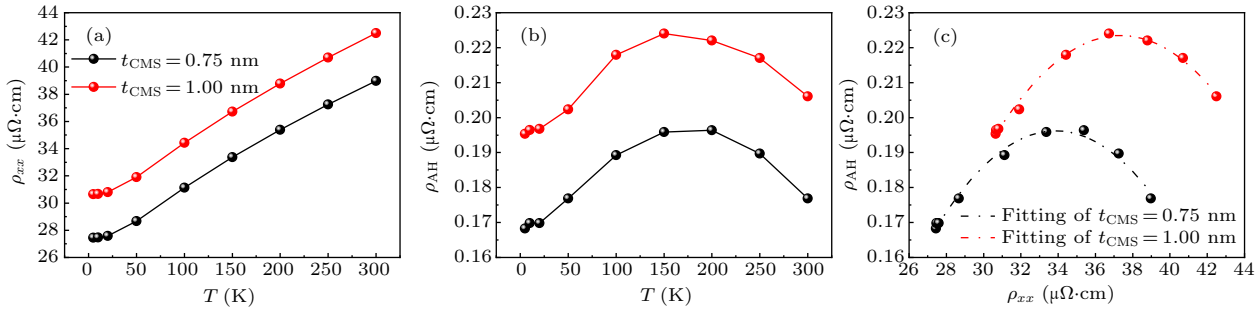

Fig. 6. (a) ρ_{xx}–T, (b) ρ_{AH}–T, and (c) ρ_{AH}–ρ_{xx} curves for Ta (6 nm)/[Pt (2 nm)/CMS (t_{CMS} nm)]$_3$/Pt (4 nm) multilayers. The black and red dash-dotted lines in panel (c) are the fitting curves.

The AHE is generally understood to arise from three main mechanisms: the intrinsic mechanism,[5] the skew-scattering mechanism,[48] and the side-jump mechanism.[49] To investigate the dominant scattering mechanisms of the AHE in Pt/CMS multilayer systems, this study focuses on samples exhibiting PMA. Based on the scaling theory proposed by Tian *et al.*,[50] a systematic study of the AHE mechanism in this multilayer system is conducted. The scaling relationship can be expressed as follows:

$$\rho_{\mathrm{AH}} = a'\rho_{xx0} + a''\rho_{xxT} + b\rho_{xx}^{2}. \tag{5}$$

Here, $\rho_{xxT} = \rho_{xx} - \rho_{xx0}$, where ρ_{xx0} is the residual resistivity, approximated by the longitudinal resistivity measured at 5 K in the experiment. The first term, $a'\rho_{xx0}$, characterizes the impurity scattering contribution in the low-temperature limit. The second term, $a''\rho_{xxT}$, accounts for the phonon-assisted skew scattering contribution. The third term, $b\rho_{xx}^{2}$, arises from the side-jump and the intrinsic mechanisms, with the latter associated with the topological Berry curvature. By fitting the ρ_{AH}–ρ_{xx} dependence, the parameters a', a'', and b are extracted, enabling a quantitative assessment of their respective contributions.

As shown in Fig. 6(c), the black and red dashed lines represent the fitting curves to Eq. (5) for $t_{\mathrm{CMS}} = 0.75$ nm ($a' = 0.0247$, $a'' = 0.0459$, $b = -6.776 \times 10^{-4}$ $\mu\Omega^{-1}\cdot\mathrm{cm}^{-1}$) and $t_{\mathrm{CMS}} = 1.00$ nm ($a' = 0.0257$, $a'' = 0.0472$, and $b = -6.320 \times 10^{-4}$ $\mu\Omega^{-1}\cdot\mathrm{cm}^{-1}$). The fitting results indicate that, in Ta/[Pt/CMS]$_3$/Pt multilayers, phonon scattering in the skew scattering mechanism is the dominant contribution to the AHE, followed by impurity scattering. The contribution of the intrinsic mechanism is small. As the CMS thickness increases from 0.75 nm to 1.00 nm, the a' and a'' coefficients increase by 4.1% and 2.8%, respectively, indicating enhanced impurity scattering due to interfacial defect accumulation and strengthened skew scattering arising from enhanced electron–phonon coupling. However, as the CMS thickness increases, the absolute value of the parameter b decreases by 6.7%, due to the relative weakening of interfacial effects and the enhanced contributions from impurity and skew scattering. This leads to a reduced relative contribution of the intrinsic scattering.

As can be seen from the above discussion, the multilayers exhibit PMA and a pronounced AHE when the ferromagnetic CMS layer thickness is 1.00 nm. Therefore, to investigate the influence of the number of periods n on the magnetic and transport properties, the CMS layer thickness was fixed at $t_{\mathrm{CMS}} = 1.00$ nm. Figures 7(a) and 7(b) present the out-of-plane and in-plane hysteresis loops of Ta (6 nm)/[Pt (2 nm)/CMS (1 nm)]$_n$/Pt (4 nm) multilayers in the as-deposited state. The out-of-plane hysteresis loops show high rectangularity with a remanence ratio $M_{\mathrm{r}}/M_{\mathrm{s}} \approx 1$, whereas the in-plane loops display a linear, non-rectangular characteristic. All samples, regardless of the number of periods n, exhibit easier magnetic saturation under a magnetic field applied perpendicular to the plane, indicating the presence of PMA. It can be clearly observed that the saturation magnetization per unit area, $M_{\mathrm{s}} \times t_{\mathrm{total(CMS)}}$, increases linearly with n, as expected from the layer-by-layer additive contribution of the CMS ferromagnetic layers. Notably, all samples exhibit very low coercivity H_{c}, with the out-of-plane H_{c} below 10 Oe for $n \geq 2$, due to strong interlayer exchange coupling mediated by the Pt spacer layer, which facilitates magnetization reversal. In addition, the in-plane remanence ratio $M_{\mathrm{r}}/M_{\mathrm{s}}$ decreases with increasing n, indicating enhanced PMA.

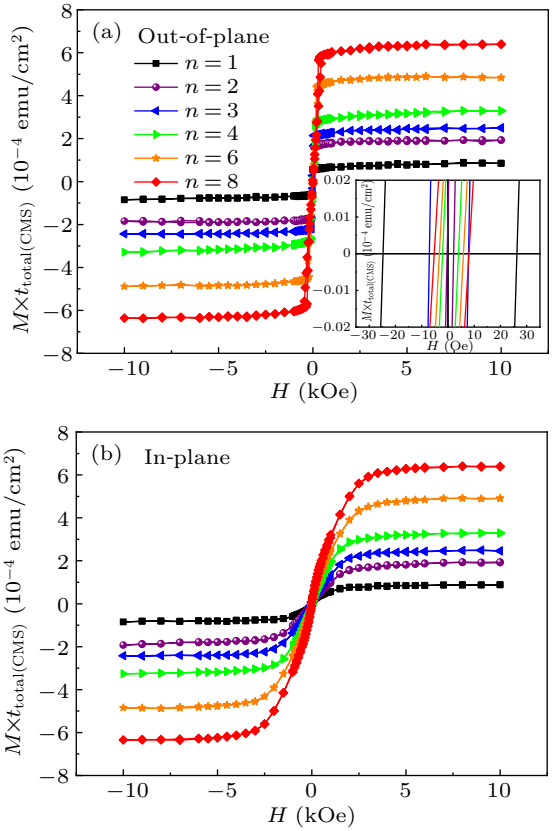

Fig. 7. (a) Out-of-plane and (b) in-plane hysteresis loops of Ta (6 nm)/[Pt (2 nm)/CMS (1 nm)]$_n$/Pt (4 nm) multilayers. The inset in panel (a) shows a magnified view around the coercive field.

Next, the influence of the number of periods n on the transport properties in Ta(6 nm) / [Pt(2 nm) / CMS(1 nm)]$_n$ / Pt(4 nm) multilayers is investigated. As shown in Fig. 8(a), ρ_{xx} shows a decreasing trend with increasing n for all measured temperatures. At low n, the total film thickness is small, enhancing surface and interface scattering and effectively reducing the electron mean free path, thereby increasing ρ_{xx}. As n increases, the total film thickness increases. This suppresses surface and interface scattering, causing the multilayers to exhibit more bulk-like behavior, thereby reducing ρ_{xx}. Meanwhile, as n increases, the number of Pt/CMS interfaces increases, enhancing SOC at the interfaces and thereby strengthening the AHE, which significantly boosts ρ_{AH}. Furthermore, increasing n leads to the accumulation of lattice mismatch and

dislocation density at the interfaces. These interfacial defects act as electron scattering centers and further contribute to the enhancement of ρ_{AH}. Consequently, as shown in Fig. 8(b), ρ_{AH} increases with increasing n across all tested temperatures. The dashed lines in Fig. 8(c) are obtained by fitting the $\rho_{AH} - \rho_{xx}$ curves to Eq. (5), showing very close agreement with the experimental data. Figure 8(d) summarizes the extracted parameters, a', a'', and b as a function of n. For all samples, phonon scattering is found to be the dominant contribution to the AHE, followed by impurity scattering, whereas the intrinsic mechanism associated with Berry curvature makes the smallest contribution. Moreover, the impurity scattering coefficient a' and the phonon scattering coefficient a'' increase with n, and the absolute value of the intrinsic parameter b also increases. As n increases, the number of Pt/CMS interfaces increases. The hybridization between Pt 5d and Co 3d orbitals at these interfaces enhances SOC, thereby amplifying impurity and phonon scattering effects. When the thickness of each individual layer is smaller than the electron mean free path, the contributions of these mechanisms to the AHE increase with the total thickness of the CMS layer.

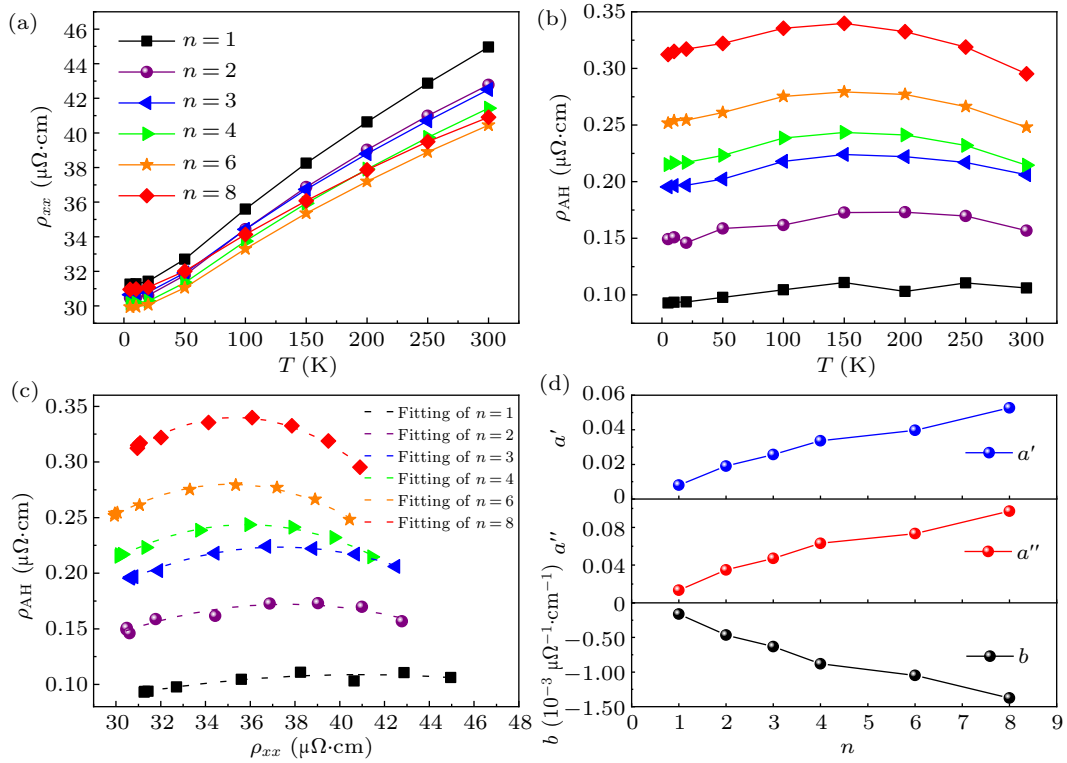

Fig. 8. (a) ρ_{xx}–T, (b) ρ_{AH}–T, and (c) ρ_{AH}–ρ_{xx} curves for Ta (6 nm)/[Pt (2 nm)/CMS (1 nm)]$_n$/Pt (4 nm) multilayers. The dashed lines in panel (c) are the fitting curves. (d) Fitting results for parameters a', a'', and b.

4. Conclusion

In summary, the influence of the ferromagnetic layer thickness t_{CMS} and the number of periods n on the PMA and electrical transport properties of Ta (6 nm)/[Pt (2 nm)/CMS (t_{CMS} nm)]$_n$/Pt (4 nm) multilayers is systematically investigated. Our results indicate that for $t_{CMS} \leq 1.00$ nm, interfacial SOC induces hybridization between Pt 5d and Co 3d orbitals, which gives rise to the PMA and results in a significantly positive effective magnetic anisotropy constant K_{eff}. In contrast, for $t_{CMS} \geq 1.25$ nm, enhanced bulk cubic anisotropy drives a transition to in-plane magnetization. As n increases from 1 to 3, the interfacial magnetic anisotropy constant K_i increases by 46.2%, indicating that periodic multilayer structures enhance the cumulative SOC through an increased number of Pt/CMS interfaces, thereby significantly strengthening the PMA. The electrical transport results reveal that phonon scattering is the dominant contribution to the AHE, with impurity scattering playing a secondary role, while the intrinsic mechanism associated with Berry curvature makes a negligible contribution. These findings offer a promising pathway toward high-density, low-power spintronic storage and sensing technologies. However, further investigation of device architectures and their scalability in practical applications is required to enable real-world implementation.

Acknowledgements

Project supported by the National Natural Science Foundation of China (Grant Nos. 52361035, 52261036, and 11964027) and the Natural Science Foundation of Ningxia Hui Autonomous Region, China (Grant No. 2023AAC03079).

References

[1] Jiang M, Yang X, Qu S, Wang C, Ohya S and Tanaka M 2024 *ACS Appl. Mater. Interfaces* **16** 23497

[2] Tadić M, Panjan M, Čekada M, Jagličić Z, Pregelj M, Spreitzer M and Panjan P 2023 *Ceram. Int.* **49** 32068

[3] Hromov A, Panjan M, Tadić M, Zorko A and Pregelj M 2024 *Acta Mater.* **279** 120320

[4] Prinz G A 1998 *Science* **282** 1660

[5] Nagaosa N, Sinova J, Onoda S and MacDonald A H 2010 *Rev. Mod. Phys.* **82** 1539

[6] Hassoun M M, Black W C, Lee E K F, Geiger R L and Hurst A 1997 *IEEE Trans. Magn.* **33** 3307

[7] Barton C W and Thomson T 2015 *J. Appl. Phys.* **118** 063901

[8] Toyama R, Kawachi S, Yamaura J I, Murakami Y, Hosono H and Majima Y 2020 *Jpn. J. Appl. Phys.* **59** 075504

[9] Zhu Y, Zhang Z, Ma B and Jin Q Y 2012 *J. Appl. Phys.* **111** 07C106

[10] Solovyev I V, Dederichs P H and Mertig I 1995 *Phys. Rev. B* **52** 13419

[11] Oogane M, Kubota T, Kota Y, Mizukami S, Naganuma H, Sakuma A and Ando Y 2010 *Appl. Phys. Lett.* **96** 252501

[12] Zhu Z, Wan Y, Long H, Wang X, Wang X, Lang L, Ma L and Zheng F 2025 *Surf. Interfaces* **57** 105800

[13] Sukegawa H, Hadorn J P, Wen Z, Ohkubo T, Mitani S and Hono K 2017 *Appl. Phys. Lett.* **110** 112403

[14] Hadorn J P, Sukegawa H, Ohkubo T, Mitani S and Hono K 2018 *Acta Mater.* **145** 306

[15] Saravanan L, Raja M M, Prabhu D, Pandiyarasan V, Ikeda H and Therese H A 2018 *J. Magn. Magn. Mater.* **454** 267

[16] Wen K, Xiu X, Jiang J, He Y, Huang F and Wang S 2019 *J. Phys. D: Appl. Phys.* **52** 485005

[17] Monso S, Rodmacq B, Auffret S, Casali G, Fettar F, Gilles B, Dieny B and Boyer P 2002 *Appl. Phys. Lett.* **80** 4157

[18] Endo M, Kanai S, Ikeda S, Matsukura F and Ohno H 2010 *Appl. Phys. Lett.* **96** 212503

[19] Takamura Y, Suzuki T, Fujino Y and Nakagawa S 2014 *J. Appl. Phys.* **115** 17C732

[20] Suzuki M, Muraoka H, Inaba Y, Miyagawa H, Kawamura N, Shimatsu T, Maruyama H, Ishimatsu N, Isohama Y and Sonobe Y 2005 *Phys. Rev. B* **72** 054430

[21] Liu L, Lee O J, Gudmundsen T J, Ralph D C and Buhrman R A 2012 *Phys. Rev. Lett.* **109** 096602

[22] Sun Y, Ba Y, Chen A, He W, Wang W, Zheng X, Zou L, Zhang Y, Yang Q, Yan L, Feng C, Zhang Q, Cai J, Wu W, Liu M, Gu L, Cheng Z, Nan C W, Qiu Z, Wu Y, Li J and Zhao Y 2017 *ACS Appl. Mater. Interfaces* **9** 10855

[23] Ma L, Zhao H, Zheng F, Wang X M, Tian N and You C Y 2025 *Appl. Surf. Sci.* **700** 163257

[24] Yu G, Chang L T, Akyol M, Upadhyaya P, He C, Li X, Wong K L, Amiri P K and Wang K L 2014 *Appl. Phys. Lett.* **105** 102411

[25] Lau Y C, Betto D, Rode K, Coey J and Stamenov P 2016 *Nat. Nanotechnol.* **11** 758

[26] Han J, Richardella A, Siddiqui S A, Finley J, Samarth N and Liu L 2017 *Phys. Rev. Lett.* **119** 077702

[27] Dieny B and Chshiev M 2017 *Rev. Mod. Phys.* **89** 025008

[28] Rawat K, Sharma A, Brajpuriya R K, Reddy V, Gloskovskii A, Kaushik V, Gupta A and Pathak S 2025 *Appl. Surf. Sci.* **697** 162952

[29] Akbulut S, Akbulut A, Özdemir M and Yildiz F 2015 *J. Magn. Magn. Mater.* **390** 137

[30] Gupta S, Sbiaa R, Al Bahri M, Ghosh A, Piramanayagam S, Ranjbar M and Akerman J 2018 *J. Phys. D: Appl. Phys.* **51** 465002

[31] Davydenko A V, Kozlov A G, Ognev A V, Stebliy M E, Samardak A S, Ermakov K S, Kolesnikov A G and Chebotkevich L A 2017 *Phys. Rev. B* **95** 064430

[32] Tudu B, Tian K and Tiwari A 2017 *Sensors* **17** 2743

[33] An G G, Lee J B, Yang S M, Kim J H, Chung W S, Yoon K S and Hong J P 2015 *AIP Adv.* **5** 027137

[34] Qin X, Tan J, Xiu X, Cao W and Wang S 2025 *Chin. Phys. B* **34** 037502

[35] Li Z, Zhang K, Du A, Zhang H, Chen W, Xu N, Hao R, Yan S, Zhao W and Leng Q 2023 *Chin. Phys. B* **32** 026803

[36] Yan C, Chen L, Zhou K, Yang L, Fu Q, Wang W, Yue W, Liang L, Tao Z, Du J, Wang Y and Liu R 2023 *Chin. Phys. B* **32** 017503

[37] Pradines B, Calmels L and Arras R 2021 *Phys. Rev. Appl.* **15** 034009

[38] Stuelke L, Kharel P, Shand P M and Lukashev P V 2021 *Phys. Scr.* **96** 125818

[39] Bai Q, Jiang J, Guo B, Cao W, Xiu X and Wang S 2022 *J. Alloys Compd.* **897** 163114

[40] Fu H, You C, Li Y, Wang K and Tian N 2016 *J. Phys. D: Appl. Phys.* **49** 195001

[41] Fu H, You C, Ma L, Tian N, Xin F, Cheng Z, Basha A and Kohn A 2018 *Phys. Rev. Mater.* **2** 124404

[42] Yuan Y, Wei L, Lu Y, Liu R, Liu T, Chen J, You B, Zhang W, Wu D and Du J 2023 *Chin. Phys. B* **32** 067505

[43] Kumar P, Sharma V, Khanna M K and Kuanr B K 2025 *Phys. Lett. A* **553** 130722

[44] Draaisma H J G, de Jonge W J M and den Broeder F J A 1987 *J. Magn. Magn. Mater.* **66** 351

[45] Vaz C A F, Bland J A C and Lauhoff G 2008 *Rep. Prog. Phys.* **71** 056501

[46] Mukherjee J, Suraj T S, Basumatary H, Sethupathi K and Raman K V 2021 *Phys. Rev. Mater.* **5** 014201

[47] Pugh E M 1930 *Phys. Rev.* **36** 1503

[48] Berger L 1970 *Phys. Rev. B* **2** 4559

[49] Smit J 1958 *Physica* **24** 39

[50] Tian Y, Ye L and Jin X 2009 *Phys. Rev. Lett.* **103** 087206